ADVANCED MATERIALS INTERFACES
Open Access
www.advmatinterfaces.de

A Predictive Model for Monolayer-Selective Metal-Mediated MoS_2 Exfoliation Incorporating Electrostatics

Alexander Corletto, Marco Fronzi, Alexis Krywula Joannidis, Peter C. Sherrell, Michael J. Ford, David A. Winkler, Joseph G. Shapter, James Bullock, and Amanda V. Ellis**

The metal-mediated exfoliation (MME) method enables monolayer-selective exfoliation of van der Waals (vdW) crystals, improving the efficacy of large monolayer production. Previous physical models explaining monolayer-selective MME propose that the main contributors to monolayer-selectivity are vdW crystal/metal surface binding energy and/or vdW crystal layer strain resulting from lattice mismatch. However, the performance of some metals for MME is inconsistent with these models. Here, a new model is proposed using MoS_2 as a representative vdW crystal. The model explains how the MoS_2/metal interface electrostatics, in combination with strain, determines monolayer-selectivity of MME by modulating the MoS_2 interlayer energy. Monolayer MoS_2/metal interfaces are characterized using in situ Raman spectroscopy and density functional theory calculations to estimate the electrostatics and strain of MoS_2 in contact with different metals. The model successfully demonstrates the dependence of MME monolayer-selectivity on the MoS_2/metal interface electrostatics and highlights the significance of electrostatics in nanomaterial vdW interactions.

1. Introduction

Layered 2D van der Waals (vdW) crystals, particularly transition metal dichalcogenides (TMDCs), are emerging as ideal materials for electronic and optoelectronic devices.[1–3] Especially in their monolayer form, they exhibit fundamental advantages over conventional bulk semiconductors.[4] Therefore, reliable preparation of large, damage-free, monolayer vdW crystals is an important manufacturing goal. Metal surfaces are particularly useful for monolayer-selective exfoliation of bulk vdW crystals, vastly improving the yield of large monolayers.[5–12] Metal-mediated exfoliation (MME) enables the incorporation of pristine, millimetre-scale monolayer vdW crystals into electronic devices without the high temperatures needed for direct monolayer synthesis.[13] MME also avoids defects, common during solution exfoliation, that alter the vdW crystal electronic structure.[14] Monolayer-selective MME involves either deposition of metal onto a bulk vdW crystal,[5,10] or direct contact of the bulk vdW crystal with a clean metal surface.[6–9,11,15–17] As the bulk vdW crystal is separated from the metal surface, vdW crystals are selectively exfoliated, leaving monolayers attached to the metal surface. Molybdenum disulfide (MoS_2), the most studied vdW crystal, is a model compound for exfoliation in the large family of TMDCs. Currently, Au is the most commonly used metal

A. Corletto, J. Bullock
Department of Electrical and Electronic Engineering
The University of Melbourne
Parkville, Victoria 3010, Australia

A. Corletto, M. Fronzi, A. K. Joannidis, P. C. Sherrell, A. V. Ellis
Department of Chemical Engineering
The University of Melbourne
Parkville, Victoria 3010, Australia
E-mail: peter.sherrell@rmit.edu.au; amanda.ellis@unimelb.edu.au

M. Fronzi, M. J. Ford
School of Mathematical and Physical Science
University of Technology Sydney
Ultimo, New South Wales 2007, Australia

The ORCID identification number(s) for the author(s) of this article can be found under https://doi.org/10.1002/admi.202300686

DOI: 10.1002/admi.202300686

P. C. Sherrell
School of Science
STEM College
RMIT University
Melbourne, Victoria 3000, Australia

D. A. Winkler
Monash Institute of Pharmaceutical Sciences
Monash University
Parkville, Victoria 3052, Australia

D. A. Winkler
School of Biochemistry and Chemistry
La Trobe Institute for Molecular Science
La Trobe University
Bundoora, Victoria 3086, Australia

D. A. Winkler
School of Pharmacy
The University of Nottingham
Nottingham NG7 2RD, UK

J. G. Shapter
Australian Institute for Bioengineering and Nanotechnology
The University of Queensland
Brisbane, Queensland 4072, Australia

for MME due to its high monolayer-selectivity.[5–9,15,17] Other metals, including Pd, Ag, Pt, Ni, and Cu, have also been successfully used.[10,11,16] Despite its widespread use, the physical mechanism of monolayer-selective MME is still unclear, suggesting additional scope for fully exploiting MME.

A seminal model of MME proposed that monolayer-selectivity was due to the strong binding between the Au surface and S atoms on the surface of MoS_2, comparable to covalent-like surface Au-thiol bonding.[5,7] Accordingly, efficient monolayer-selectivity was due to the strength of the Au-MoS_2 bonds and the relative weakness of the MoS_2 vdW interlayer bonding. However, this model does not explain how cleaving preferentially occurs between the 1st and 2nd MoS_2 layers on the Au surface (MoS_2(1), MoS_2(2), respectively).[5,7] Cleaving occurs preferentially at interfaces with lower binding energy, yet the model does not suggest any difference in MoS_2 interlayer binding energy. To address this limitation, a second model proposed that lattice mismatch strain in MoS_2(1) in contact with a metal surface is the main contributor to monolayer-selectivity in MME.[16,18] Strain reduces the atomic density of the MoS_2(1) layer and/or increases the interlayer distance, reducing the attractive vdW interactions between MoS_2(1) and MoS_2(2). Indeed, Au applies a significant tensile strain to MoS_2 (up to 5.5%)[19] that may weaken the MoS_2(1)/MoS_2(2) interlayer binding energy and facilitate monolayer-selective MME.[16] However, this second model cannot explain observations by Johnston & Khondaker[10] concerning monolayer-selective MME on metal surfaces that apply negligible strain to MoS_2, such as Pd.[10] The authors hypothesized that the large binding energy between MoS_2 and Pd facilitates monolayer-selectivity, similar to the first model, yet this does not explain the preferential cleavage at the MoS_2(1)/MoS_2(2) interface. Additionally, directly-deposited Al has a high binding energy and large lattice mismatch/applied strain, yet exhibits poor monolayer-selectivity,[10] inconsistent with the predictions of either model. The experimental results suggest that the current models are incomplete, and a new model is required that addresses the modulation of MoS_2(1)/MoS_2(2) interlayer binding energy in contact with different metal surfaces.

Here, we present such a model that elucidates how the electrostatics of the MoS_2(1)/metal interface, in combination with strain from lattice mismatch, modulates the monolayer-selectivity of MME by directly modulating the MoS_2(1)/MoS_2(2) interlayer energy. This model lays the foundation for a theory that can predict monolayer selectivity of MME, enabling highly efficient and fully controlled production of large monolayer vdW structures. The model also has important implications for understanding electrostatic modulation of vdW interactions and its impact on manipulation of nanomaterials. The model has resulted from a thorough investigation of the electrostatics of the MoS_2/metal interface. In situ characterization of these interfaces is experimentally challenging so data in the literature is sparse, and indirect electronic methods can perturb the interface.[20] Fortunately, modulation of electron density and strain in monolayer MoS_2 (1L-MoS_2) can be measured by changes in Raman spectra, allowing direct in situ characterization of 1L-MoS_2 in contact with metals, with negligible interference to the MoS_2/metal interface.[9,17,21] MoS_2/metal interface properties such as the built-in potential and lattice mismatch strain can then be derived from measured 1L-MoS_2 properties. Here, we report experimental in situ Raman spectroscopy characterization of 1L-MoS_2/metal interfaces for a variety of metals. Changes in the 1L-MoS_2 electron density and strain are used to derive the built-in potential and strain at the MoS_2 surface of MoS_2/metal interfaces. This elucidates the mechanism of monolayer-selective MME of MoS_2. Density functional theory (DFT) calculations of MoS_2/metal interfaces support the experimental measurements of the interface electrostatics and determine how the modulation of MoS_2 interlayer energy from electric fields depends on the structure and electron distribution of the material.

2. Results and Discussion

2.1. Raman Analysis of 1L-MoS_2 in Contact with Metals

The Raman spectrum of MoS_2 has two distinct modes, A_1' and E', corresponding to out-of-plane and in-plane Raman-active vibrational modes (**Figure 1**A). The Raman shift of both modes is dependent on the electron density and strain in the MoS_2 sample.[22] Fortunately, the A_1' mode is more sensitive to electron density[23] and the E' mode to strain.[24–27] The relationship between A_1' and E' Raman shifts and electron density and strain can be expressed as,[21]

$$\omega_{A_1'} = \omega^0_{A_1'} - 2\gamma_{A_1'}\omega^0_{A_1'}\varepsilon + k_{A_1'}\Delta n_e \quad (1)$$

$$\omega_{E'} = \omega^0_{E'} - 2\gamma_{E'}\omega^0_{E'}\varepsilon + k_{E'}\Delta n_e \quad (2)$$

where: Δn_e is the change in electron density in 1L-MoS_2 and ε is the strain applied to 1L-MoS_2; $\omega_{A_1'}$ and $\omega^0_{A_1'}$ are the modulated and intrinsic Raman shift of the A_1' mode Raman peak, respectively; $\omega_{E'}$ and $\omega^0_{E'}$ are the modulated and intrinsic Raman shift of the E' mode Raman peak, respectively; $k_{A_1'}$ and $k_{E'}$ are the electron density constants that specify the changes in Raman shift from Δn_e;[23] and $\gamma_{A_1'}$ and $\gamma_{E'}$ are the Grüneisen parameters that specify the change in Raman shift from ε.[25] The measured values of $\gamma_{A_1'}$ and $\gamma_{E'}$ are ≈0.21 and 0.68, respectively[28] consistent with previous studies.[22,23,25–27] The electron density constants $k_{A_1'} = -2.2 \times 10^{13}$ cm^{-2} and $k_{E'} = -0.33 \times 10^{13}$ cm^{-2} have been found previously by fitting experimental data.[21,23] Suspended 1L-MoS_2, with no contact with any other material (aside from ambient air), was used as the reference, with $\varepsilon = 0\%$ and $\Delta n_e = 0$. Lloyd et al.[28] measured the E' Raman mode peak at 385 cm^{-1} and the A_1' Raman mode peak at 405 cm^{-1} for suspended 1L-MoS_2, which we use as the reference (Figure 1A). The different characteristic Raman vibrational mode peaks that were fitted on the Raman spectra of 1L-MoS_2/metal interfaces are listed in **Table 1**.

Here, metal films (except Al) were deposited via thermal or electron-beam evaporation physical vapor deposition (PVD) directly onto a bulk MoS_2 crystal, followed by monolayer-selective MME of the bulk MoS_2 to reveal the 1L-MoS_2/metal interface (details in Experimental Section; Section S1 and Figure S1, Supporting Information). Here, direct deposition of the metal film on to bulk MoS_2 via PVD was preferred to the transfer method,[32] as the PVD approach ensured no oxidation of the metal surface[16] or impurity contamination[6] occurred at the 1L-MoS_2/metal interface. While some damage to MoS_2 may occur during PVD metal

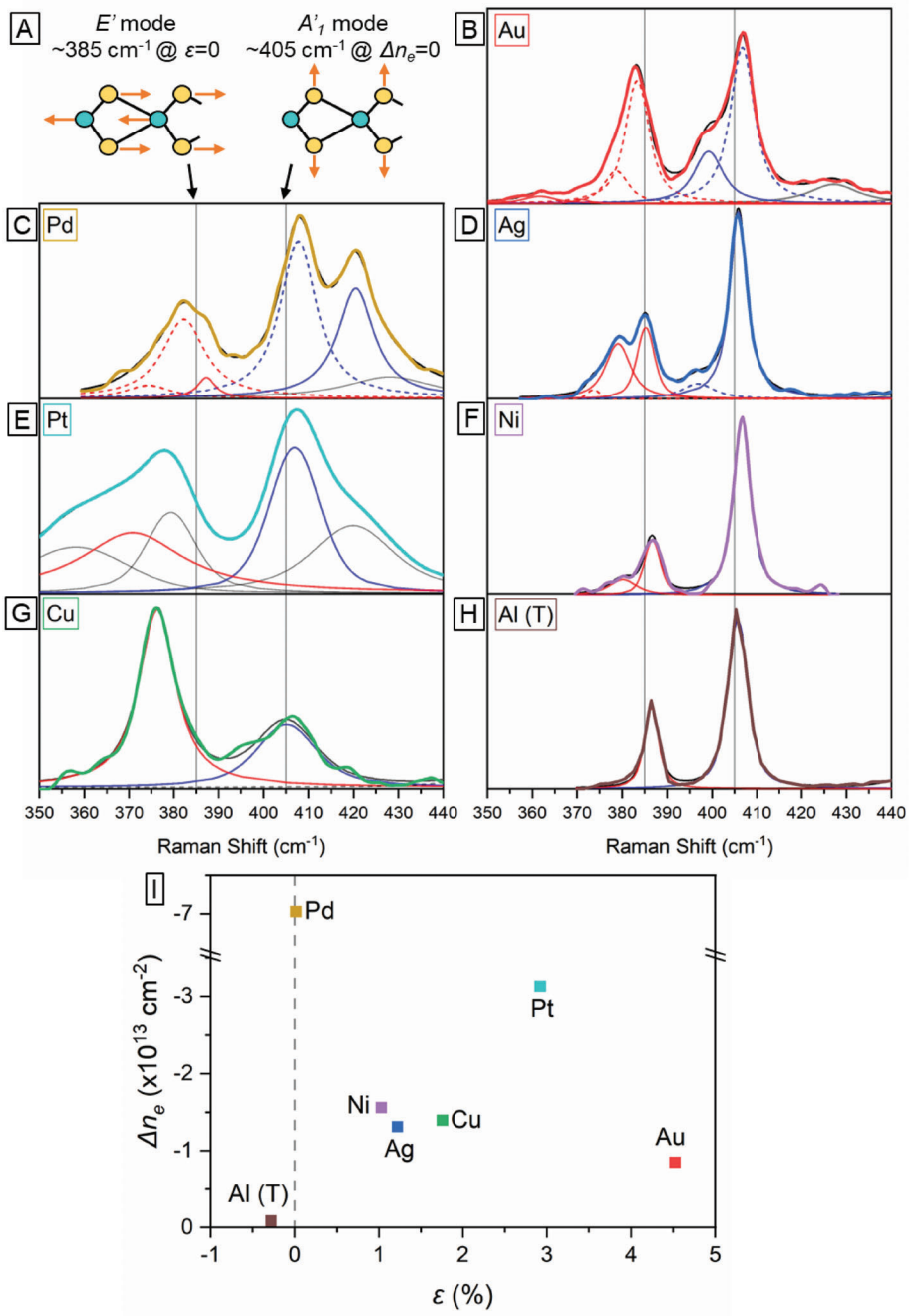

Figure 1. A) In-plane, E', and out-of-plane, A_1', Raman-active fundamental vibrational modes of 1L-MoS_2 that have intrinsic (unmodulated) Raman shifts of 385 and 405 cm^{-1}, respectively. B–G) Non-resonant Raman spectra of 1L-MoS_2 contacting Au, Pd, Ag, Pt, Ni, or Cu films, respectively, prepared by direct PVD of metals on bulk MoS_2, and performing MME. H) Non-resonant Raman spectra of 1L-MoS_2 contacting Al film obtained by standard mechanical exfoliation on an Al film, labelled as Al (T). Spectra were obtained with a 532 nm excitation wavelength. A_1' mode peaks and E' mode peaks are blue and red, respectively. Peaks marked with dashes are from a secondary region of the 1L-MoS_2/metal interface. Other Raman-active vibrational mode peaks are grey. Raman spectra are normalized to the maximum intensity peak within each spectrum. I) Δn_e versus percentage ε of the 1L-MoS_2 at the various 1L-MoS_2/metal interfaces, calculated from the respective measured Raman spectra peaks.

deposition,[32,33] it can be accounted for by fitting the disorder activated LA(M), LO(M), and TO(M) modes if they appear in the Raman spectra (Table 1). Al films could not achieve monolayer-selectivity, so MoS_2 was directly exfoliated onto a freshly deposited Al film on a Si/SiO_2 substrate under inert atmosphere (glovebox) and a small 1L-MoS_2 flake was used to characterize the 1L-MoS_2/Al interface. Figure 1B–H (Supporting Information) shows the Raman spectra obtained from 1L-MoS_2 samples in contact with different metal films and the Voigt profile-fitted characteristic Raman vibrational mode peaks. MoS_2 Raman peaks are

Table 1. Peak positions and descriptions of the Raman mode peaks of interest for characterizing the 1L-MoS_2/metal interfaces.

Raman-active Vibrational Mode	Raman Spectrum Peak Position (cm^{-1})	Description
E'	385	Fundamental lateral vibrational mode. Red shifts under tensile strain and blue shifts under compressive strain.[21,27]
E^- and E^+	<385	Split E' vibrational modes due to strain-induced lattice symmetry breaking.
A_1'	405	Fundamental vertical vibrational mode. Red shifts when electron density increases and blue shifts when electron density decreases.[21,27]
2LA(M)	450	Second order longitudinal acoustic mode at M point. Weak intensity.[27,29]
LA(≈K)+ TA(≈K)	428	Linear combination of the longitudinal acoustic mode and transverse acoustic mode at K point. Very weak intensity.[27,30]
LA(M)	227	Longitudinal acoustic mode at M point. Significant disorder-activated and intensity proportional to defect density in 1L-MoS_2.[31]
LO(M)	377	Longitudinal optical mode at M point. Only activated from significant crystal lattice disorder.[31]
TO(M)	358	Transverse optical mode at M point. Only activated from significant crystal lattice disorder.[31]

fitted with Voight spectral profiles to incorporate the intrinsic Lorentzian peak profile and the instrumental-dependant Gaussian peak profile.[22,26,28] All Raman spectra shown in Figure 1B–H represent an average of >4 points across the 1L-MoS_2/metal interface and are normalized to the maximum peak intensity of each spectrum (only relative intensity between peaks of the same spectrum is considered). Figure 1I (Supporting Information) plots ϵ and Δn_e of each 1L-MoS_2/metal interface, calculated from the E' (or E^-) and A_1' mode Raman peaks. Figure S2 (Section S2, Supporting Information) also plots E' (or E^-) against A_1' mode Raman peak positions for each 1L-MoS_2/metal interface with reference lines to visualise the change of ϵ and Δn_e. The fitted peak data and resulting calculated 1L-MoS_2 ϵ and Δn_e from all samples are summarized in **Table 2**.

1L-MoS_2 in contact with directly deposited Au, Ag, and Ni films exhibited measurable splitting of the E' mode peak (Figure 1B,D,F). This splitting has been reported previously in 1L-MoS_2 with >1% uniform uniaxial tensile strain and likely occurs at lower ϵ, although the split peaks are challenging to distinguish clearly.[24] E' mode peak splitting is due to symmetry breaking under uniaxial tensile strain that changes the crystallographic point group from *D3h* to *Cs*.[24,35,36] Lateral E' mode lattice vibrations parallel (E^-) and perpendicular (E^+) to the applied strain are no longer degenerate. This indicates that 1L-MoS_2 is under uniaxial tensile strain when in contact with these metal films due to lattice mismatch. The Grüneisen parameters for the change of E' mode Raman shift due to ϵ, are calibrated on the split E' mode that correlates with the ϵ direction. Thus, the E^- mode peak is used to determine 1L-MoS_2 ϵ and Δn_e from the Raman spectra with split E^- mode peaks. The E^- mode peaks for the measured samples are lower in intensity than the E^+ mode peaks, in contrast to previous observations of uniaxially strained MoS_2.[24] However, in these samples ϵ was applied via lattice mismatch of a strongly interacting metal film. Thus, the metal film will interfere with the 1L-MoS_2 vibrational modes and suppress the E' mode peaks.[19]

1L-MoS_2/Au also exhibits splitting of the A_1' mode peak, with an observable small shoulder (A_1^1) at 399.2 cm^{-1} on the peak (A_1^2) at 406.7 cm^{-1} (Figure 1B). This has been observed previously in heterogeneous MoS_2/metal interfaces where the metal did not contact the whole MoS_2 surface, or regions of the interface varied.[9,36] Inhomogeneous distribution of Au directly deposited on MoS_2 by PVD may cluster into non-uniform Au nanostructures on the MoS_2 surface (island growth kinetics),[37]

Table 2. Voight profile peaks fitted to the 1L-MoS_2/metal Raman spectra for the E' (or split E^- and E^+) and A_1' Raman modes, electron density change (Δn_e) and strain (ϵ) calculated from the Raman peaks, metal work function (Φ_m),[34] ideal (Φ_i) and measured (Φ_Δ) built-in potential for the 1L-MoS_2/metal interface, and the DFT-calculated charge transfer (negative for electron depletion and positive for electron accumulation in the metal substrate) and binding energy of the 1L-MoS_2/metal interface.

	E' Peak [cm^{-1}]	E^- Peak [cm^{-1}]	E^+ Peak [cm^{-1}]	A_1' Peak [cm^{-1}]	Δn_e (10^{13} cm^{-2})	ϵ (%)	Φ_m [eV]	Φ_i [eV]	Φ_Δ [eV]	Charge Transfer (DFT) [e $Å^{-2}$]	Binding Energy (DFT) [eV $Å^{-2}$]
Au	–	361.6	370.9	399.2	−0.85	4.52	5.1	0.14	0.13	−0.005	−0.098
Pd	387.2	–	–	420.4	−7.03	0.02	5.6	1.27	1.11	−0.029	−0.139
Ag	–	379.0	385.2	405.8	−1.31	1.22	4.74	0.24	0.21	−0.010	−0.095
Pt	370.7	–	–	406.9	−3.13	2.92	5.9	1.16	0.50	−0.018	−0.151
Ni	–	380.1	386.7	406.7	−1.56	1.03	5.01	0.54	0.25	−0.039	−0.196
Cu	376.3	–	–	405.1	−1.39	1.76	4.7	0.12	0.22	−0.012	−0.129
Al (T)	386.5	–	–	405.7	−0.08	−0.28	4.22	−0.07	0.01	0.018	−0.204

resulting in nanoscale MoS_2 regions in close contact with an Au grain and other MoS_2 regions "suspended" at a further distance from the Au surface between the Au grains. Crystalline Au(111) interfacing with 1L-MoS_2 may also create moiré superstructures that result in heterogeneous 1L-MoS_2/Au interfaces and different regions with varying interactions.[38] These result in a heterogenous metal-MoS_2 interface that will cause additional splitting of the A_1' and E' mode peaks, corresponding to the different regions that cause distinct ϵ and Δn_e.[9] A lower intensity $A_1{}^1$ mode peak compared to the $A_1{}^2$ mode peak may indicate intimate MoS_2/metal contact or high ϵ causing severe Raman intensity suppression.[19] The split E' mode peaks corresponding to $A_1{}^1$ will also have low intensities that make it difficult to observe in the Raman spectrum. The reduced intensity of the E' modes corresponding to $A_1{}^1$ can obscure them under other E' modes and previous literature may have overlooked the additional splitting of E' mode peaks for this reason.[20] A small Raman peak in the deconvoluted Raman spectra at 361.6 cm^{-1} was assigned to the E^- mode corresponding to $A_1{}^1$. Using the $A_1{}^1$ and corresponding E^- mode peaks (Table 2) to define the primary 1L-MoS_2/Au interface region allowed estimation of $\epsilon = 4.5\%$ and $\Delta n_e = -0.85 \times 10^{13}$ cm^{-2}, consistent with recent experimental reports and theoretical ϵ from the Au-MoS_2 lattice mismatch (6.3%).[17,19,20,39]

For the 1L-MoS_2/Pd interface, the A_1' mode peak is split into two large prominent peaks at 407.8 and 420.4 cm^{-1} (Figure 1C). The peak at 420.4 cm^{-1}, although having a large Raman shift, is not due to the LA(≈K)+ TA(≈K) modes because its FWHM of 9.9 cm^{-1} is too small for these phonon modes in non-resonance Raman.[30] Additionally, the 2LA(M) mode peak should be more intense than the LA(≈K)+TA(≈K) mode peak for 1L-MoS_2 in non-resonant or resonant Raman spectra.[29] However, in the 1L-MoS_2/Pd interface Raman spectrum, the 420.4 cm^{-1} peak is more intense than the 2LA(M) mode peak. Further, the peak observed at 428.0 cm^{-1} is less intense and possesses a much larger FWHM of 24.0 cm^{-1} and is thus identified here as the LA(≈K)+TA(≈K) combination peak. Pd deposition on MoS_2 has been reported to exhibit island growth with very small atomic clusters with ⟨111⟩ direction interfacing with the MoS_2.[40] This creates a heterogeneous interface, similar to the1L-MoS_2/Au interface, and can explain the A_1' mode peak splitting. The Pd islands are preferentially limited to very small 7 atom clusters, so the Pd film surface still has very low roughness.[40] The interface region between the islands will have increased interface distance and reduced binding energy, and will thus have different ϵ and Δn_e values. The primary 1L-MoS_2/Pd regions (Pd < 111 > island face on MoS_2) have a measured $\epsilon = 0.02\%$, expected from the small lattice mismatch between 1L-MoS_2 and Pd (≈0.5%)[37] and similar to previous reports.[40]

Raman peaks that are assigned to the secondary interface region for the 1L-MoS_2/Au and 1L-MoS_2/Pd samples along with their calculated Δn_e and ϵ are presented in Section S2 (Supporting Information). 1L-MoS_2/Ag exhibited similar splitting of the A_1' mode peak. A small secondary A_1' mode peak at 396.8 cm^{-1} was observable indicating a secondary 1L-MoS_2/Ag interface, as previously reported for this interface.[36,37,41] However, we found that the corresponding E^- mode peak for the secondary 1L-MoS_2/Ag interface was too small to be accurately deconvoluted from the obtained Raman spectra, so the secondary interface region could not be measured for the 1L-MoS_2/Ag sample.

The E' mode peak in the 1L-MoS_2/Cu interface Raman spectrum has a greater intensity than the A_1' mode peak, in contrast to the greater intensity A_1' mode peak for every other metal. Additionally, there is no splitting of the E' mode peak. More intense, non-split E' mode peak is indicative of a uniform biaxial strain experienced by the 1L-MoS_2 at the 1L-MoS_2/Cu interface.[28] Small Δn_e and strain were measured from the transferred 1L-MoS_2/Al interface. Small strain is expected for transferred contacts as the larger gap between the MoS_2 and metal layers inevitably results in a weaker interaction and between the layers and less possible total strain being applied.[17]

Introducing significant defects in the 1L-MoS_2 crystal lattice causes the appearance of the LA(M) mode peak at ≈227 cm^{-1}, and the intensity is proportional to the defect density.[31] LA(M) mode peak is only observable in the 1L-MoS_2/Pt Raman spectra which indicates that only this interface has significant defects introduced to the 1L-MoS_2. Broadening of E′ and A′$_1$ mode peaks in 1L-MoS_2/Pt Raman spectra is also characteristic of damage defects.[31] Pt deposition may have caused damage to MoS_2 due to the high energy required for electron beam PVD. The Raman peaks at 379.3 and 358.1 cm^{-1} are assigned as the disorder-activated LO(M) and TO(M), respectively, leaving the Raman peak at 370.7 cm^{-1} assigned as the E′ mode peak. The 2LA(M) mode peak at ≈450 cm^{-1} is observable in most of the 1L-MoS_2/metal spectra.[29,42]

The measured ϵ and Δn_e were then used to derive the Schottky junction built-in potential (Φ_Δ) and the interfacial charge transfer.

2.2. Schottky Junction Formation, Charge Transfer, and Induced Strain During MME

When the metal work function (Φ_M) is larger than the Fermi energy (E_F) of the semiconductor, electrons transfer from the MoS_2 semiconductor to the metal and Schottky junctions can form at the MoS_2/metal interface (**Figure 2**A). This causes electron depletion in the semiconducting MoS_2 layer (see further discussion in Section S3, Supporting Information).[43,44] Indeed, the 1L-MoS_2/metal interfaces reduced the electron density ($\Delta n_e < 0$) of the 1L-MoS_2 (Figure 1I), suggesting formation of Schottky junctions.[39] A correlation is observed between the ideal built-in potential (Φ_i) and Δn_e, where Φ_i is calculated as follows:

$$\Phi_i = \Phi_M - X_{MoS_2} - \left(E_F - E_C\right) \quad (3)$$

where X_{MoS_2} is the 1L-MoS_2 electron affinity, and E_F and E_C are the Fermi level and conduction band minimum, respectively.

The effects of 1L-MoS_2 strain are also important. The X_{MoS_2} of 4.33 eV can be increased by ~0.14 eV per 1% tensile strain, resulting in a reduced Φ_i and consequently reduced Δn_e in the MoS_2.[45,46] Sulfur vacancy (V_S) defects cause n-type doping in 1L-MoS_2 with a defect density (N_d) of ~10^{13} cm^{-2}.[47–49] N_d is highest (~10^{19} cm^{-3}) on ambient exposed surfaces of MoS_2, constituting highly n-doped 1L-MoS_2.[50] PVD deposition of metal films also creates additional V_S in the MoS_2 surface relative to the

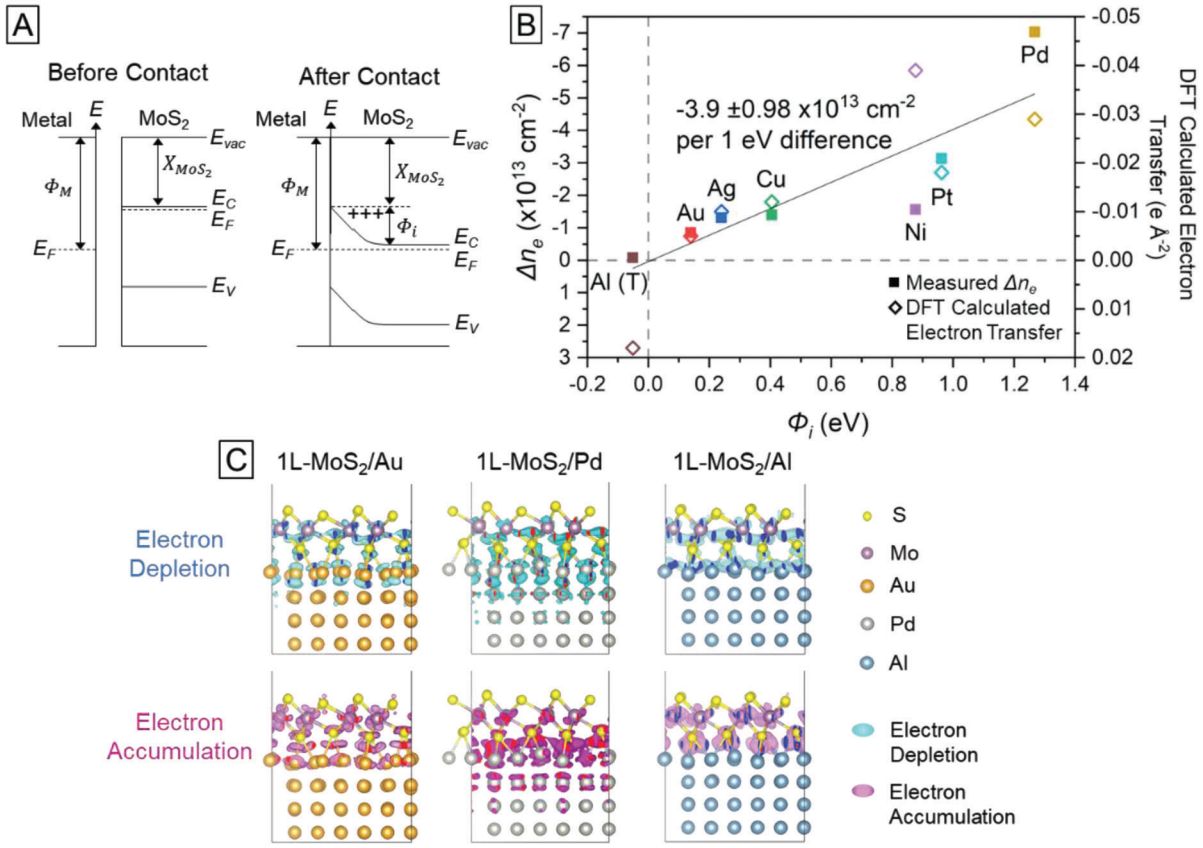

Figure 2. A) Schematic of the band structure of typical n-type MoS_2 and a metal surface, before and after contact, showing the formation of a Schottky junction. Electrons are depleted from the MoS_2 and transfer to the metal to maintain a constant electrochemical potential across the interface, resulting in band bending at the interface and an in-built potential at the MoS_2 surface. B) Raman spectra-determined Δn_e for the different 1L-MoS_2/metal interfaces against their ideal built-in potential (Φ_i) (filled squares), showing increased electron depletion with greater Φ_i. The interfacial electron transfer obtained by DFT calculations is also plotted against Φ_i, showing a similar trend. C) 3D rendering of the DFT calculations of the 1L-MoS_2/metal interfaces and visualization of the electron redistribution at the interface. 1L-MoS_2/Au, 1L-MoS_2/Pd, and 1L-MoS_2/Al interfaces are exhibited left to right. Blue and magenta volumes indicate electron depletion and accumulation, respectively (brightness does not indicate depletion/accumulation magnitude).

suspended 1L-MoS_2 reference. V_S for the 1L-MoS_2 sample used was confirmed by energy dispersive X-ray spectroscopy (EDX) measurements. This indicated a ~1:1.7 Mo:S stoichiometry compared to 1:2 for pristine MoS_2 (Section S4, Supporting Information). Due to this high defect density on the MoS_2 surfaces we estimate that E_F -$E_C \approx 0$.[50,51] Consequently, Φ_i for these samples can be calculated as,

$$\Phi_i = \Phi_M - \left(X_{MoS_2} + (0.14\epsilon\%)\right) \quad (4)$$

Figure 2B plots the Raman spectra-determined Δn_e against Φ_i. The Φ_M of the < 111> surface was used for each metal (Table 2), except for Au where the Φ_M of a polycrystalline surface was used due to its island growth on MoS_2 surface producing an inhomogeneous interface (See Section S2, Supporting Information).[34,37,40] A linear correlation was observed between Δn_e and Φ_i, consistent with Schottky-Mott theory that states larger Φ_i values increase electron depletion. The actual built-in potentials (Φ_Δ) at the MoS_2 surface in contact with the metals were calculated from Δn_e (Table 2; and Section S5, Supporting Information). The calculated pinning factor S was ≈0.64, suggesting that only partial Fermi level pinning has occurred for these 1L-MoS_2/metal interfaces, similar to that predicted by Gong et al (S = 0.71).[39,52] A Δn_e value of $-3.9 \pm 0.98 \times 10^{13}$ cm^{-2} per 1 eV Φ_i was measured. The 1L-MoS_2/Au interface induced only a small reduction in electron density, indicative of a small built-in potential and Schottky barrier. This correlates well to the lower measured contact resistivity for Au/MoS_2 reported in the literature,[53] and demonstrates the impact of the large strain of the Au/MoS_2 interface reducing the built-in potential.

2.3. Corroboration from Density Functional Theory Calculations

DFT calculations using a vdW correlation-corrected GGA functional were performed to validate the charge transfer at the 1L-MoS_2/metal interfaces (Figure 2C). 1L-MoS_2/metal interfaces were chosen to be studied via DFT (rather than 2L-MoS_2/metal or periodic MoS_2/metal interfaces) to enable direct comparison with the samples measured by Raman spectroscopy. From these DFT 1L-MoS_2/metal interfaces, the net charge transfer along the z-direction was calculated with respect to the x-y plane located at the interface. The calculated values correlate well with the experimental Δn_e values and are approximately linearly

related to Φ_i (Figure 2B and Table 2). This suggests that the charge redistribution is mainly driven by the Schottky junction and that the Schottky-Mott rule holds at the atomic scale for the 1L-MoS_2/metal interface. The 1L-MoS_2/Au interface was calculated to have the smallest electron transfer from the 1L-MoS_2 to a metal film. This small electron transfer matches the small negative Δn_e measured experimentally from the primary 1L-MoS_2/Au interface region. The calculations showed that, in 1L-MoS_2/Al, there was a net transfer of electrons into MoS_2 ($\Delta n_e > 0$), opposite to the other metals. This is due to the smaller Φ_M of Al compared to 1L-MoS_2 E_F that drives electron accumulation in 1L-MoS_2 (Figure 2C). The Δn_e and ϵ values from Raman spectra and DFT calculations were used to determine Φ_Δ for the MoS_2/metal interfaces. The change in $MoS_2(1)/MoS_2(2)$ interlayer energy as a function of Φ_Δ and ϵ could then be determined.

2.4. Model for Electrostatics-Enabled, Monolayer-Selective MME

We propose that metal surfaces in contact with bulk MoS_2 and other semiconductor TMDCs enable monolayer-selective MME by reducing electron density in $MoS_2(1)$ and shifting electron distribution away from the interlayer through electric fields. This reduces attractive vdW interactions at the $MoS_2(1)/MoS_2(2)$ interface (**Figure 3**A) and works in combination with with reduced attractive vdW interactions caused by strain. Electric fields have been shown previously to reduce attractive vdW interactions in MoS_2 and other molecules by removing electron density from the interlayer and increasing effective interlayer distance.[54,55] Metal surfaces can reduce electron density in bulk MoS_2 and form an electric field that increases effective $MoS_2(1)/MoS_2(2)$ interlayer distances by forming a Schottky junction that redistributes charge in the bulk MoS_2 (Figure 3B). The resulting interlayer binding energy (E_{Int}) can be written as,

$$E_{Int} = E_{Int0} + \Delta E_{Int}(\epsilon) + \Delta E_{Int}(E) + \Delta E_{Int}(n) \tag{5}$$

The initial interlayer energy (E_{Int0}) is modulated by the strain-induced change in $MoS_2(1)$ atomic density and the $MoS_2(1)/MoS_2(2)$ interlayer distance ($\Delta E_{\mathrm{Int}}(\epsilon)$), the Schottky electric field-induced change in effective $MoS_2(1)/MoS_2(2)$ interlayer distance ($\Delta E_{Int}(E)$), and the electron density-induced change in polarizability ($\Delta E_{Int}(n)$).

It is well known that atomic registry mismatch strain increases interlayer distance and the distance for minimum energy, depending on the structure of the vdW crystal.[18] Sun et al.[18] calculated a reduction in E_{Int} for bilayer MoS_2 of ≈0.0025 eV Å^{-2} for $\epsilon = 5\%$ in the MoS_2 top layer, which is used to estimate a linear $E_{Int}(\epsilon)$,

$$\Delta E_{Int}(\epsilon) = \epsilon_{\%} \times 5 \times 10^{-4}\ \mathrm{eV\ \AA^{-2}} \tag{6}$$

To determine the structure-dependent $\Delta E_{Int}(E)$, geometry-optimized calculations of bilayer MoS_2 with applied electric fields were performed with the vdW correlation-corrected GGA functional to model the effect of the Schottky-induced electric field at the $MoS_2(1)/MoS_2(2)$ interlayer (Section S6, Supporting Information). An $\Delta E_{Int}(E)$ of ≈0.001 eV Å^{-2} for an out-of-plane applied field of 0.016 eV Å^{-1} or 1.6×10^6 V cm^{-1} was calculated. To calculate the Schottky junction-induced electric field at the $MoS_2(1)/MoS_2(2)$ interface, the depletion region width in MoS_2 is first calculated using the full depletion approximation as[56]

$$x_d = \sqrt{\frac{2\epsilon_s\left(\Phi_i - V_a\right)}{qN_d}} \tag{7}$$

where N_d is the defect density, and V_a is applied bias across the interface. Using $N_d = \sim 10^{19}$ cm^{-3} [50] and dielectric constant of MoS_2 as ~4,[54] no applied bias, and using our calculated Φ_Δ from the measured Δn_e in 1L-MoS_2 (Table 2) we can obtain,

$$x_d = \sqrt{\frac{2\epsilon_s\Phi_\Delta}{qN_d}} = \sqrt{\frac{2\times 4\times 8.85\times 10^{-14}}{1.602\times 10^{-19}\times 10^{19}}}\sqrt{\Phi_\Delta}$$
$$= \left(6.65\times 10^{-7}\right)\sqrt{\Phi_\Delta}\ \mathrm{cm} \tag{8}$$

Schottky junction-induced electric field at the $MoS_2(1)/MoS_2(2)$ interface is then calculated as,[56]

$$E(x) = \frac{qN_d}{\epsilon_s}\left(x_d - x_t\right) \tag{9}$$

where x_t is the distance from the MoS_2/metal interface to the $MoS_2(1)/MoS_2(2)$ interface, which is the 1L-MoS_2 thickness (0.7 nm).[57] Equation 9 can then be expanded using Equation 8 as,

$$E(0.7\ \mathrm{nm}) = \frac{qN_d}{\epsilon_s}\left(\left(6.65\times 10^{-7}\right)\sqrt{\Phi_\Delta} - 0.7\times 10^{-7}\right)$$
$$= \frac{1.602\times 10^{-19}\times 10^{19}}{4\times 8.85\times 10^{-14}}\left(\left(6.65\times 10^{-7}\right)\sqrt{\Phi_\Delta} - 0.7\times 10^{-7}\right)$$
$$\cong \left(3.0\sqrt{\Phi_\Delta} - 0.32\right)\times 10^6\ \mathrm{V\ cm^{-1}} \tag{10}$$

Thus, the relationship of $\Delta E_{Int}(E)$ at the $MoS_2(1)/MoS_2(2)$ interface due to Φ_Δ is,

$$\Delta E_{Int}(E) \cong \frac{\left(3.0\sqrt{\Phi_\Delta} - 0.32\right)\times 10^6\ \mathrm{V\ cm^{-1}}}{1.6\times 10^6\ \mathrm{V\ cm^{-1}}} \times 0.001\ \mathrm{eV\ \AA^{-2}}$$
$$= \left(1.9\sqrt{\Phi_\Delta} - 0.20\right)\times 10^{-3}\ \mathrm{eV\ \AA^{-2}} \tag{11}$$

Equation 7 shows that applying a bias across the MoS_2/metal interface can modulate x_d and consequently $E(x)$ and $\Delta E_{Int}(E)$. This suggests that the interlayer vdW attraction of the $MoS_2(1)/MoS_2(2)$ interface can be precisely controlled via an applied bias. This presents a great opportunity for applications involving precise exfoliation or manipulation of monolayer vdW crystals. These equations also highlight that x_d and thus the electric field extends 2.4–7 nm into the MoS_2 for Φ_Δ between 0.13–1.11 eV, reducing E_{Int} for a few MoS_2 interlayers. However, the electric field is still strongest nearest the MoS_2/metal interface and the $MoS_2(1)/MoS_2(2)$ interface will have the greatest reduction in E_{Int} to enhance monolayer-selective MME efficacy.

$\Delta E_{Int}(n)$ is a highly complex function that depends on the change of polarizability of the MoS_2 layers due to changes in

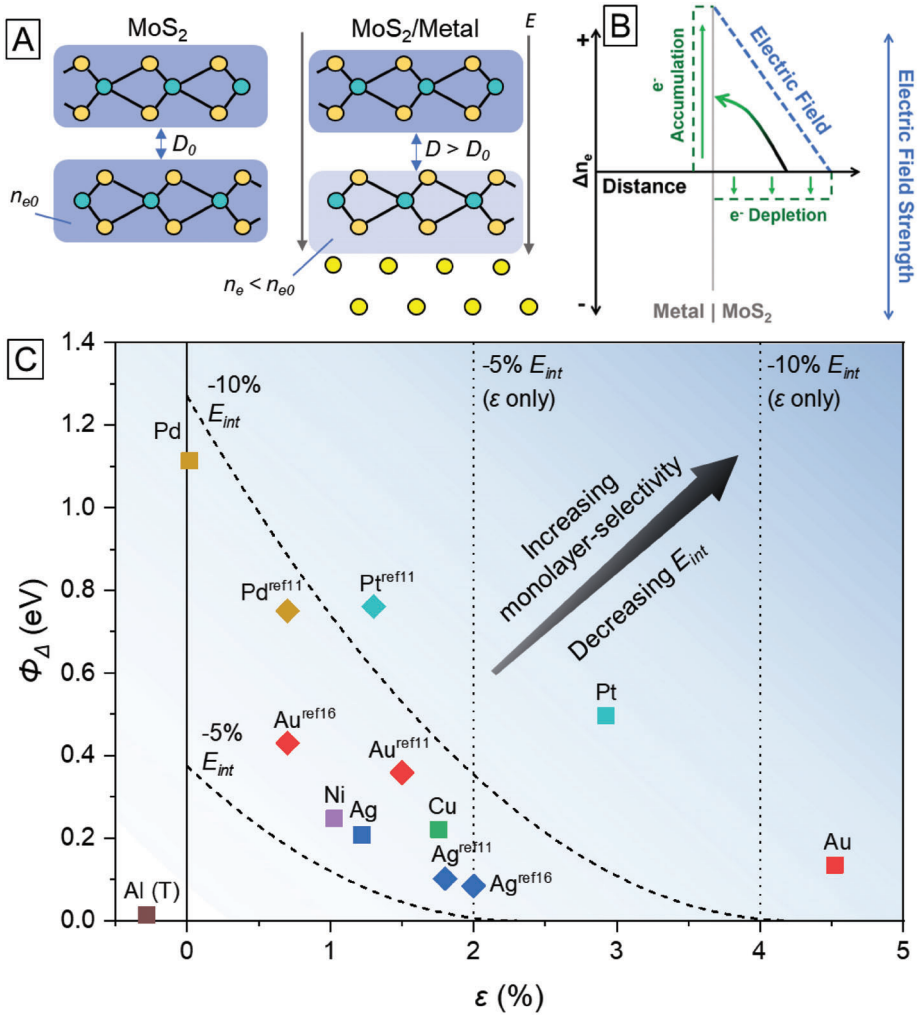

Figure 3. A) Simplified schematic of the MoS_2/metal Schottky junction causing reduced interlayer energy/vdW interactions. The Schottky-induced electric field distorts the electron distribution and increases the effective interlayer distance (D), consequently reducing vdW interactions. The electron depletion/reduced electron density (n_e) results in reduced polarizability that reduces vdW interactions. B) Electrostatics of the MoS_2/metal Schottky junction using the full depletion approximation. Electron density (n_e) (green dashes) is reduced in the MoS_2 (right side) and equally increased in the metal (left side). An electric field (blue dashes) is established in the MoS_2 depletion width (x_d), with maximum strength near the interface. The y-axis is the change in electron density (Δn_e) or electric field strength, and the x axis is the distance from the interface with the x = 0 as the MoS_2/metal interfacial plane. C) Comparison of the properties of 1L-MoS_2/metal interfaces that are predicted to enable monolayer-selective MME and the experimental attempts with different 1L-MoS_2/metal interfaces. Square data points are from this study and diamond data points are derived from the literature.[11,16] Al could not enable monolayer-selective MME in this study similar to that reported in the literature, so the transferred 1L-MoS_2 on Al film is displayed instead labelled "Al (T)". The dashed grey lines show the 1L-MoS_2/metal interface properties that result in 5% or 10% reduction in interlayer binding energy (E_{Int}) at the MoS_2(1)/MoS_2(2) interface according to the proposed model from Equation 14. Dotted grey lines show 5% or 10% reduction in E_{Int} from strain effects only ($\Delta E_{Int}(\epsilon)$).

the electron density and is dependent on the band structure and geometry of the crystals (Section S7, Supporting Information). Mannebach et al.[58] proposed a simplified model based on Lifshitz theory that estimates $\Delta E_{Int}(n)$ in TMDCs by the Casimir force. The TMDCs layers are assumed to fit the Drude model (resistivity due to scattering of electrons by metal ions) for their dielectric function when they have high free electron density. This Lifshitz model agrees with more detailed many-body computational models, such as electron-hole fluid superlattice models that account for near-field effects, and the adiabatic connection fluctuation dissipation theorem within random phase approximation.[58–60] It is applicable to surface MoS_2 because the high surface doping causes large free electron density. This model calculates $\Delta E_{Int}(n)$ from the change of volumetric charge carrier density (Δn) as,

$$\Delta E_{Int}(n) \cong -\frac{\hbar e}{64\pi l^2\sqrt{2m\epsilon_0}}\sqrt{\Delta n} \tag{12}$$

where m is the effective electron mass, e is the elementary charge, and l is the Mo-Mo interlayer distance. Larger n increases attractive interlayer vdW interactions. Using the full depletion approximation ($\Delta n_e = N_d = 10^{19}$ cm^{-3}),[50] m of MoS_2 of 0.45, l of ≈6.2 Å,[58] and assuming a Schottky junction on MoS_2(1),

$\Delta E_{\mathrm{Int}}(n)$ of the $MoS_2(1)/MoS_2(2)$ interface can be obtained as (full derivation in Section S8, Supporting Information),

$$\Delta E_{Int}(n) \cong 1.6 \times 10^{-5}\ \mathrm{eV}\ \forall^{-2} \tag{13}$$

The Casimir force change in $\Delta E_{Int}(n)$ at the $MoS_2(1)/MoS_2(2)$ interface is likely stronger than estimated by Equation 13, because the highly-doped, metal-like, surface MoS_2 can transition to a poor conductor (low free electron density) after electron depletion from the Schottky junction, however we do not account for that change here.[51,60,61]

Equations 6, 11, and 13 can be substituted into Equation 5 to obtain an estimate of E_{Int} at the $MoS_2(1)/MoS_2(2)$ interface based on the Φ_Δ and ϵ in $MoS_2(1)$,

$$E_{Int} = \left(-19.4 + 0.5\epsilon_{\%} + 1.9\sqrt{\Phi_\Delta} - 0.18\right) \times 10^{-3}\ \mathrm{eV}\ \forall^{-2} \tag{14}$$

Figure 3C plots the measured Φ_Δ and ϵ for the 1L-MoS_2/metal interfaces from this study and from the literature for comparison (see Section S9, Supporting Information for all values).[11,16] Dashed lines denoting a 5% and 10% reduction in the $MoS_2(1)/MoS_2(2)$ E_{Int} are based on Equation 14. $E_{Int0} = -0.0\ 1936$ eV Å^{-2} was calculated from the MoS_2 bilayer calculation (Section S6, Supporting Information).

The effective monolayer-selective MME of bulk MoS_2 with Pd demonstrates that monolayer-selectivity is not solely due to $\Delta E_{Int}(\epsilon)$, as MoS_2/Pd interfaces have small strain ($\epsilon < 0.5\%$) that causes negligible $\Delta E_{Int}(\epsilon)$. Rather the positive $\Delta E_{Int}(E)$ and $\Delta E_{Int}(n)$ values explain the effective monolayer-selective MME using Pd surfaces. The ineffectiveness of monolayer-selective MME of bulk MoS_2 using directly-deposited Al is also not solely explained by $\Delta E_{Int}(\epsilon)$, as the large lattice mismatch between Al $< 111 >$ and 1L-MoS_2 (≈5%) should produce a large ϵ that reduces E_{Int}.[39] Additionally, the binding/adsorption energy for 1L-MoS_2/Al interfaces is high (−0.20 eV Å^{-2}), which was previously proposed to increase monolayer-selective MME effectiveness.[10] Instead, the negative $\Delta E_{Int}(E)$ and $\Delta E_{Int}(n)$ of the MoS_2/Al interface from the model offset the effect of $\Delta E_{Int}(\epsilon)$, resulting in unchanged or greater E_{Int}. This is in contrast to prior literature models that propose that the binding energy and strain between the 1L-MoS_2/metal interface are the only factors reducing attractive interlayer vdW interactions.[10]

The examples of Pd and Al exemplify how the Schottky junction-induced electron depletion and electric fields in MoS_2/metal interfaces reduce E_{Int} and facilitate monolayer-selective MME, in synergy with strain effects from lattice mismatch. The trends we observed are consistent with reports of metal MME in literature (Table S3, Supporting Information). The proposed model can effectively estimate the reduction in E_{Int} due to the MoS_2/metal interface properties. The model further suggests that E_{Int} could be precisely controlled by an applied bias across the MoS_2/metal interface, increasing monolayer-selectivity and allowing switching from adhesion to exfoliation regimes. Electronic control of the vdW crystal E_{Int} could vastly improve the effectiveness and efficiency of monolayer-selective MME and/or manipulation of monolayer vdW crystals towards device fabrication.

3. Conclusion

Different 1L-MoS_2/metal interfaces were characterized in situ using Raman spectroscopy and DFT calculations to estimate the electrostatics and strain of MoS_2 in contact with metals. Schottky junctions at the 1L-MoS_2/metal interfaces caused electron depletion/accumulation in 1L-MoS_2 and a built-in potential. A model is proposed that explains how the electrostatics of the MoS_2/metal interface acts synergistically with applied strain to determine monolayer-selectivity of MME by modulating the MoS_2 interlayer vdW interactions. The model estimates a change in MoS_2 interlayer energy from the measured MoS_2/metal interface electrostatics and strain that correlates with the monolayer-selectivity of metals for bulk MoS_2 MME. The model demonstrates the significance of electrostatics in modulating nanomaterial vdW interactions and the potential for precise electronic control of vdW interactions for nanomaterial exfoliation and manipulation. The principles underlying the model will provide significant impact beyond MME, including understanding the impact of electrostatics on vdW interactions in materials, and designing ohmic contacts for optoelectronic devices, sensing systems, and vdW heterostructures.

4. Experimental Section

Fabrication of 1L-MoS_2/Metal Interfaces (Direct Deposition Method): Bulk MoS_2 crystal, naturally sourced and purified, was supplied by 2D Semiconductors (AZ, USA). The bulk MoS_2 crystal was adhered to low-tack clean room tape. 100 nm of either Au, Pd, Ag, Pt, Ni, Cu, or Al was directly deposited onto the exposed face of the bulk MoS_2 by PVD at $<10^{-6}$ torr. Pd, Ag, Pt, Ni, and Al metals were deposited using an Angstrom Engineering Thin Film Deposition System and Au and Cu were deposited using a Thermionics e-Beam +D5:D27 Evaporator system. Au, Pd, Pt, and Cu were evaporated with an electron beam and Ag, Ni, and Al were thermally evaporated. Deposition rate was 0.1 Å s^{-1} for the first 5 nm and then ≈1 Å s^{-1} thereafter to reduce damage to the MoS_2. MME was then performed; thermal release tape was applied and adhered to the deposited metal film face (of the tape/MoS_2/metal sample) and pulled off, thereby monolayer-selectively exfoliating the MoS_2 and resulting in a large yield of 1L-MoS_2 on the metal adhered to the thermal release tape (except for Al). The exposed 1L-MoS_2 on the metal film was then characterized.

Fabrication of 1L-MoS_2/Al Interface (Transfer Method): 100 nm of Al was directly deposited onto a Si/SiO_2 wafer substrate by PVD at $<10^{-7}$ torr using an Angstrom Engineering Thin Film Deposition System. Immediately after deposition and opening of the deposition chamber (<20 s), bulk MoS_2 was applied to the fresh Al film surface and firmly pressed for 1 min to exfoliate the bulk MoS_2 onto the Al film. The deposition chamber opens into a controlled atmosphere glovebox (<100 ppm O_2, ≈0 ppm H_2O) preventing exposure of the Al film surface to ambient atmosphere and reducing any potential oxidation. The bulk MoS_2 crystal was then slowly removed, with exfoliated MoS_2 flakes remaining on the Al film. The proportion of 1L-MoS_2 exfoliated was extremely low; almost all exfoliated MoS_2 flakes on the Al film were multilayer.

Raman Spectroscopy Characterization and Analysis of 1L-MoS_2/Metal Interfaces: Raman spectroscopy characterization of the 1L-MoS_2 in contact with metal films was performed using a Renishaw InVia Raman Spectroscopy Microscope. Excitation was at 532 nm with a typical 1% power. Spectra were accumulated at single points on the 1L-MoS_2 samples for 10 s and 20 repetitions using 1800 cm^{-1} grating. Raman spectra were obtained from 4–10 different locations on a 1L-MoS_2/metal sample and averaged to produce the 1L-MoS_2/metal interface Raman spectra, displayed in Figure 1, and used for analysis. Averaging was necessary to reduce noise in the spectra due to the low intensity of the peaks and to reduce errors

from interface defects generated during fabrication. Raman spectra were normalized to the maximum peak intensity of each spectrum. Voight peak profiles were fitted to the Raman spectra to obtain the Raman mode peaks.

DFT analysis of MoS_2/Metal Interfaces and MoS_2 Bilayer: Periodic Density Functional Theory (DFT) calculations were implemented in the Vienna Ab Initio Simulation Package (VASP), within the generalized gradient approximation (GGA) for the exchange correlation functional, as formulated by Perdew and Wang (PBE).[62–64] A van der Waals correlation correction was applied using the method of Grimme, with Becke–Jonson damping.[65,66] Projector augmented-wave (PAW) potentials were used to describe the core-valence interaction with the valence electrons described by periodic plane waves with cut-off energy of 520 eV. The convergence criteria used for energy and forces on each atom was 10^{-6} eV and 10^{-2} eV Å^{-1}, respectively. The charge transfer, from and to the metallic substrate, had been calculated considering the charge included within the Wigner-Seitz atomic radius.

Optical Microscopy and X-ray Spectroscopy of 1L-MoS_2/Metal Interfaces: Optical microscope images of the 1L-MoS_2/metal samples were obtained using an Olympus BH2-UMA optical microscope with 50x objective and NIS Elements acquisition software.

Energy dispersive X-ray spectroscopy of the 1L-MoS_2/Pd interface sample was obtained with a Hitachi FlexSEM 1000 using the EDX mode with a XFlash 5010 detector. Data was acquired with 15 keV beam energy at 30° take-off angle, 25 s acquisition time, 10.5 mm working distance, and ≈150 µm x 200 µm scan area.

Supporting Information

Supporting Information is available from the Wiley Online Library or from the author.

Acknowledgements

A.C., M.F., D.A.W., J.G.S., and A.V.E. acknowledge support from the Australian Research Council Discovery Project Scheme, grant number: DP200101217. P.C.S. acknowledges support from the Elizabeth & Vernon Puzey Foundation via the Elizabeth & Vernon Puzey Fellowship at the University of Melbourne, and support from RMIT University via the Vice-Chancellor's Research Fellowship Scheme. This work was performed in part at the Materials Characterisation and Fabrication Platform (MCFP) at the University of Melbourne and the Victorian Node of the Australian National Fabrication Facility (ANFF).

Open access publishing facilitated by The University of Melbourne, as part of the Wiley – The University of Melbourne agreement via the Council of Australian University Librarians.

Conflict of Interest

The authors declare no conflict of interest.

Data Availability Statement

The data that support the findings of this study are available from the corresponding author upon reasonable request.

Keywords

2D materials, exfoliation, molybdenum disulfide, raman spectroscopy, transition metal dichalcogenides, van der Waals

Received: August 17, 2023
Revised: September 28, 2023
Published online:

[1] D. Lembke, S. Bertolazzi, A. Kis, *Acc. Chem. Res.* **2015**, *48*, 100.
[2] J. Bullock, M. Amani, J. Cho, Y.-Z. Chen, G. H. Ahn, V. Adinolfi, V. R. Shrestha, Y. Gao, K. B. Crozier, Y.-L. Chueh, A. Javey, *Nat. Photonics* **2018**, *12*, 601.
[3] X. Guan, X. Yu, D. Periyanagounder, M. R. Benzigar, J.-K. Huang, C.-H. Lin, J. Kim, S. Singh, L. Hu, G. Liu, D. Li, J.-H. He, F. Yan, Q. J. Wang, T. Wu, *Adv. Opt. Mater.* **2021**, *9*, 2001708.
[4] A. Chaves, J. G. Azadani, H. Alsalman, D. R. da Costa, R. Frisenda, A. J. Chaves, S. H. Song, Y. D. Kim, D. He, J. Zhou, A. Castellanos-Gomez, F. M. Peeters, Z. Liu, C. L. Hinkle, S.-H. Oh, P. D. Ye, S. J. Koester, Y. H. Lee, P. Avouris, X. Wang, T. Low, *npj 2D Mater. Appl.* **2020**, *4*, 29.
[5] S. B. Desai, S. R. Madhvapathy, M. Amani, D. Kiriya, M. Hettick, M. Tosun, Y. Zhou, M. Dubey, J. W. Ager, D. Chrzan, A. Javey, *Adv. Mater.* **2016**, *28*, 4053.
[6] M. Velický, G. E. Donnelly, W. R. Hendren, S. McFarland, D. Scullion, W. J. I. DeBenedetti, G. C. Correa, Y. Han, A. J. Wain, M. A. Hines, D. A. Muller, K. S. Novoselov, H. D. Abruña, R. M. Bowman, E. J. G. Santos, F. Huang, *ACS Nano* **2018**, *12*, 10463.
[7] Y. Huang, Y.-H. Pan, R. Yang, L.-H. Bao, L. Meng, H.-L. Luo, Y.-Q. Cai, G.-D. Liu, W.-J. Zhao, Z. Zhou, L.-M. Wu, Z.-L. Zhu, M. Huang, L.-W. Liu, L. Liu, P. Cheng, K.-H. Wu, S.-B. Tian, C.-Z. Gu, Y.-G. Shi, Y.-F. Guo, Z. G. Cheng, J.-P. Hu, L. Zhao, G.-H. Yang, E. Sutter, P. Sutter, Y.-L. Wang, W. Ji, X.-J. Zhou, et al., *Nat. Commun.* **2020**, *11*, 2453.
[8] F. Liu, W. Wu, Y. Bai, S. H. Chae, Q. Li, J. Wang, J. Hone, X.-Y. Zhu, *Science* **2020**, *367*, 903.
[9] M. Velický, A. Rodriguez, M. Bouša, A. V. Krayev, M. Vondráček, J. Honolka, M. Ahmadi, G. E. Donnelly, F. Huang, H. D. Abruña, K. S. Novoselov, O. Frank, *J. Phys. Chem. Lett.* **2020**, *11*, 6112.
[10] A. C. Johnston, S. I. Khondaker, *Adv. Mater. Interfaces* **2022**, *9*, 2200106.
[11] M. Heyl, S. Grützmacher, S. Rühl, G. Ligorio, N. Koch, E. J. W. List-Kratochvil, *Adv. Mater. Interfaces* **2022**, *9*, 2200362.
[12] M. Heyl, E. J. W. List-Kratochvil, *Appl. Phys. A* **2022**, *129*, 16.
[13] Y. Zhang, Y. Yao, M. G. Sendeku, L. Yin, X. Zhan, F. Wang, Z. Wang, J. He, *Adv. Mater.* **2019**, *31*, 1901694.
[14] S. Ippolito, P. Samorì, *Small Sci.* **2022**, *2*, 2100122.
[15] M. Heyl, D. Burmeister, T. Schultz, S. Pallasch, G. Ligorio, N. Koch, E. J. W. List-Kratochvil, *Phys. Status Solidi RRL* **2020**, *14*, 2000408.
[16] M. Velický, G. E. Donnelly, W. R. Hendren, W. J. I. DeBenedetti, M. A. Hines, K. S. Novoselov, H. D. Abruña, F. Huang, O. Frank, *Adv. Mater. Interfaces* **2020**, *7*, 2001324.
[17] S. E. Panasci, E. Schilirò, G. Greco, M. Cannas, F. M. Gelardi, S. Agnello, F. Roccaforte, F. Giannazzo, *ACS Appl. Mater. Interfaces* **2021**, *13*, 31248.
[18] H. Sun, E. W. Sirott, J. Mastandrea, H. M. Gramling, Y. Zhou, M. Poschmann, H. K. Taylor, J. W. Ager, D. C. Chrzan, *Phys. Rev. Mater.* **2018**, *2*, 094004.
[19] K. Jo, P. Kumar, J. Orr, S. B. Anantharaman, J. Miao, M. J. Motala, A. Bandyopadhyay, K. Kisslinger, C. Muratore, V. B. Shenoy, E. A. Stach, N. R. Glavin, D. Jariwala, *ACS Nano* **2021**, *15*, 5618.
[20] E. Pollmann, S. Sleziona, T. Foller, U. Hagemann, C. Gorynski, O. Petri, L. Madauß, L. Breuer, M. Schleberger, *ACS Omega* **2021**, *6*, 15929.
[21] S. E. Panasci, E. Schilirò, F. Migliore, M. Cannas, F. M. Gelardi, F. Roccaforte, F. Giannazzo, S. Agnello, *Appl. Phys. Lett.* **2021**, *119*, 093103.
[22] A. Michail, N. Delikoukos, J. Parthenios, C. Galiotis, K. Papagelis, *Appl. Phys. Lett.* **2016**, *108*, 173102.
[23] B. Chakraborty, A. Bera, D. V. S. Muthu, S. Bhowmick, U. V. Waghmare, A. K. Sood, *Phys. Rev. B* **2012**, *85*, 161403.
[24] H. J. Conley, B. Wang, J. I. Ziegler, R. F. Haglund, S. T. Pantelides, K. I. Bolotin, *Nano Lett.* **2013**, *13*, 3626.

[25] C. Rice, R. J. Young, R. Zan, U. Bangert, D. Wolverson, T. Georgiou, R. Jalil, K. S. Novoselov, *Phys. Rev. B* **2013**, *87*, 081307.
[26] Y. Wang, C. Cong, C. Qiu, T. Yu, *Small* **2013**, *9*, 2857.
[27] Y. Cai, J. Lan, G. Zhang, Y.-W. Zhang, *Phys. Rev. B* **2014**, *89*, 035438.
[28] D. Lloyd, X. Liu, J. W. Christopher, L. Cantley, A. Wadehra, B. L. Kim, B. B. Goldberg, A. K. Swan, J. S. Bunch, *Nano Lett.* **2016**, *16*, 5836.
[29] X. Zhang, X.-F. Qiao, W. Shi, J.-B. Wu, D.-S. Jiang, P.-H. Tan, *Chem. Soc. Rev.* **2015**, *44*, 2757.
[30] B. R. Carvalho, Y. Wang, S. Mignuzzi, D. Roy, M. Terrones, C. Fantini, V. H. Crespi, L. M. Malard, M. A. Pimenta, *Nat. Commun.* **2017**, *8*, 14670.
[31] S. Mignuzzi, A. J. Pollard, N. Bonini, B. Brennan, I. S. Gilmore, M. A. Pimenta, D. Richards, D. Roy, *Phys. Rev. B* **2015**, *91*, 195411.
[32] Y. Liu, J. Guo, E. Zhu, L. Liao, S.-J. Lee, M. Ding, I. Shakir, V. Gambin, Y. Huang, X. Duan, *Nature* **2018**, *557*, 696.
[33] K. Schauble, D. Zakhidov, E. Yalon, S. Deshmukh, R. W. Grady, K. A. Cooley, C. J. McClellan, S. Vaziri, D. Passarello, S. E. Mohney, M. F. Toney, A. K. Sood, A. Salleo, E. Pop, *ACS Nano* **2020**, *14*, 14798.
[34] H. B. Michaelson, *J. Appl. Phys.* **2008**, *48*, 4729.
[35] C. R. Zhu, G. Wang, B. L. Liu, X. Marie, X. F. Qiao, X. Zhang, X. X. Wu, H. Fan, P. H. Tan, T. Amand, B. Urbaszek, *Phys. Rev. B* **2013**, *88*, 121301.
[36] Y. A. Moe, Y. Sun, H. Ye, K. Liu, R. Wang, *ACS Appl. Mater. Interfaces* **2018**, *10*, 40246.
[37] C. Gong, C. Huang, J. Miller, L. Cheng, Y. Hao, D. Cobden, J. Kim, R. S. Ruoff, R. M. Wallace, K. Cho, X. Xu, Y. J. Chabal, *ACS Nano* **2013**, *7*, 11350.
[38] S. Yasuda, R. Takahashi, R. Osaka, R. Kumagai, Y. Miyata, S. Okada, Y. Hayamizu, K. Murakoshi, *Small* **2017**, *13*, 1700748.
[39] C. Gong, L. Colombo, R. M. Wallace, K. Cho, *Nano Lett.* **2014**, *14*, 1714.
[40] T. E. Kidd, S. Scott, S. Roberts, R. Carlile, P. V. Lukashev, A. J. Stollenwerk, *J. Appl. Phys.* **2021**, *129*, 174303.
[41] Y. Sun, K. Liu, X. Hong, M. Chen, J. Kim, S. Shi, J. Wu, A. Zettl, F. Wang, *Nano Lett.* **2014**, *14*, 5329.
[42] G. L. Frey, R. Tenne, M. J. Matthews, M. S. Dresselhaus, G. Dresselhaus, *Phys. Rev. B* **1999**, *60*, 2883.
[43] B.-K. Kim, T.-H. Kim, D.-H. Choi, H. Kim, K. Watanabe, T. Taniguchi, H. Rho, J.-J. Kim, Y.-H. Kim, M.-H. Bae, *npj 2D Mater. Appl.* **2021**, *5*, 9.
[44] K. Noori, F. Xuan, S. Y. Quek, *npj 2D Mater. Appl.* **2022**, *6*, 73.
[45] Q. Wang, B. Deng, X. Shi, *Phys. Chem. Chem. Phys.* **2017**, *19*, 26151.
[46] B. Liu, L.-J. Wu, Y.-Q. Zhao, L.-Z. Wang, M.-Q. Cai, *Phys. Chem. Chem. Phys.* **2015**, *17*, 27088.
[47] H. Qiu, T. Xu, Z. Wang, W. Ren, H. Nan, Z. Ni, Q. Chen, S. Yuan, F. Miao, F. Song, G. Long, Y. Shi, L. Sun, J. Wang, X. Wang, *Nat. Commun.* **2013**, *4*, 2642.
[48] F. Giannazzo, G. Fisichella, A. Piazza, S. Agnello, F. Roccaforte, *Phys. Rev. B* **2015**, *92*, 081307.
[49] J. Hong, Z. Hu, M. Probert, K. Li, D. Lv, X. Yang, L. Gu, N. Mao, Q. Feng, L. Xie, J. Zhang, D. Wu, Z. Zhang, C. Jin, W. Ji, X. Zhang, J. Yuan, Z. Zhang, *Nat. Commun.* **2015**, *6*, 6293.
[50] M. D. Siao, W. C. Shen, R. S. Chen, Z. W. Chang, M. C. Shih, Y. P. Chiu, C.-M. Cheng, *Nat. Commun.* **2018**, *9*, 1442.
[51] B. Radisavljevic, A. Kis, *Nat. Mater.* **2013**, *12*, 815.
[52] C. Kim, I. Moon, D. Lee, M. S. Choi, F. Ahmed, S. Nam, Y. Cho, H.-J. Shin, S. Park, W. J. Yoo, *ACS Nano* **2017**, *11*, 1588.
[53] B. Radisavljevic, A. Radenovic, J. Brivio, V. Giacometti, A. Kis, *Nat. Nanotechnol.* **2011**, *6*, 147.
[54] E. J. G. Santos, E. Kaxiras, *ACS Nano* **2013**, *7*, 10741.
[55] A. Kleshchonok, A. Tkatchenko, *Nat. Commun.* **2018**, *9*, 3017.
[56] J. Van Zeghbroeck, *Principles of Semiconductor Devices*, Bart Van Zeghbroeck, University of Colorado, CO **2011**.
[57] A. Splendiani, L. Sun, Y. Zhang, T. Li, J. Kim, C.-Y. Chim, G. Galli, F. Wang, *Nano Lett.* **2010**, *10*, 1271.
[58] E. M. Mannebach, C. Nyby, F. Ernst, Y. Zhou, J. Tolsma, Y. Li, M.-J. Sher, I.-C. Tung, H. Zhou, Q. Zhang, K. L. Seyler, G. Clark, Y. Lin, D. Zhu, J. M. Glownia, M. E. Kozina, S. Song, S. Nelson, A. Mehta, Y. Yu, A. Pant, B. Aslan, A. Raja, Y. Guo, A. Dichiara, W. Mao, L. Cao, S. Tongay, J. Sun, D. J. Singh, et al., *Nano Lett.* **2017**, *17*, 7761.
[59] Y. Zhou, L. A. Pellouchoud, E. J. Reed, *2D Mater.* **2017**, *4*, 025005.
[60] J. Von Milczewski, J. R. Tolsma, *Phys. Rev. B* **2021**, *104*, 125111.
[61] E. G. Galkina, B. A. Ivanov, S. Savel'ev, V. A. Yampol'skii, F. Nori, *Phys. Rev. B* **2009**, *80*, 125119.
[62] G. Kresse, J. Hafner, *J. Phys.: Condens. Matter* **1994**, *6*, 8245.
[63] G. Kresse, D. Joubert, *Phys. Rev. B* **1999**, *59*, 1758.
[64] J. P. Perdew, K. Burke, M. Ernzerhof, *Phys. Rev. Lett.* **1996**, *77*, 3865.
[65] S. Grimme, J. Antony, S. Ehrlich, H. Krieg, *J. Chem. Phys.* **2010**, 132.
[66] S. Grimme, S. Ehrlich, L. Goerigk, *J. Comput. Chem.* **2011**, *32*, 1456.